An Examination of an Inland-Penetrating Atmospheric River Flood Event under Potential Future Thermodynamic Conditions

KELLY MAHONEY

NOAA/Earth Systems Research Laboratory, Physical Sciences Division, Boulder, Colorado

DUSTIN SWALES AND MICHAEL J. MUELLER

NOAA/Earth Systems Research Laboratory, NOAA/Cooperative Institute for Research in the Environmental Sciences, and University of Colorado Boulder, Boulder, Colorado

MICHAEL ALEXANDER

NOAA/Earth Systems Research Laboratory, Physical Sciences Division, Boulder, Colorado

MIMI HUGHES

NOAA/Earth Systems Research Laboratory, NOAA/Cooperative Institute for Research in the Environmental Sciences, and University of Colorado Boulder, Boulder, Colorado

KELSEY MALLOY

Rosenstiel School of Marine and Atmospheric Science, University of Miami, Miami, Florida

(Manuscript received 1 March 2018, in final form 30 April 2018)

ABSTRACT

Atmospheric rivers (ARs) are well-known producers of precipitation along the U.S. West Coast. Depending on their intensity, orientation, and location of landfall, some ARs penetrate inland and cause heavy rainfall and flooding hundreds of miles from the coast. Climate change is projected to potentially alter a variety of AR characteristics and impacts. This study examines potential future changes in moisture transport and precipitation intensity, type, and distribution for a high-impact landfalling AR event in the U.S. Pacific Northwest using an ensemble of high-resolution numerical simulations produced under projected future thermodynamic changes.

Results indicate increased total precipitation in all future simulations, although there is considerable model spread in both domain-averaged and localized inland precipitation totals. Notable precipitation enhancements across inland locations such as Idaho's Sawtooth Mountain Range are present in four out of six future simulations. The most marked inland precipitation increases are shown to occur by way of stronger and deeper moisture transport that more effectively crosses Oregon's Coastal and Cascade mountain ranges, essentially ''spilling over'' into the Snake River Valley and fueling orographic precipitation in the Sawtooth Mountains. Moisture transport enhancements are shown to have both thermodynamic and dynamic contributions, with both enhanced absolute environmental moisture and localized lower- and midlevel dynamics contributing to amplified inland moisture penetration. Precipitation that fell as snow in the present-day simulation becomes rain in the future simulations for many mid- and high-elevation locations, suggesting potential for enhanced flood risk for these regions in future climate instances of similar events.

I. Introduction

The U.S. West Coast experiences intense rainfall events from landfalling atmospheric rivers (ARs), which are long and narrow regions of intense water vapor transport (Newell et al. 1992). Depending on their intensity, orientation, and location of landfall, some ARs

Supplemental information related to this paper is available at the Journals Online website: https://doi.org/10.1175/JCLI-D-18-0118.s1.

Corresponding author: Kelly M. Mahoney, kelly.mahoney@noaa.gov

DOI: 10.1175/JCLI-D-18-0118.1

penetrate inland and cause heavy rainfall and flooding hundreds of miles from the coast (e.g., Leung and Qian 2009; Alexander et al. 2015; Rutz et al. 2014, 2015; Swales et al. 2016). Case studies of inland-penetrating AR events have shown the impacts to be largely determined by a combination of AR intensity, the specific inland-penetrating moisture pathway realized, the rain–snow line determined by environmental freezing level height, and additional local meso- and microscale processes (e.g., Neiman et al. 2008; Neiman et al. 2013; Hughes et al. 2014; Mueller et al. 2017).

In November 2006, a landfalling AR generated record-breaking precipitation across the Pacific Northwest, with the largest amounts falling in western Washington and Oregon in the region of the Olympic and Cascade Mountains; strong inland moisture transport allowed for heavy precipitation in the interior northwest as well. Notably, record rainfall and destructive flooding occurred 800 km inland at Montana's Glacier National Park (GNP; Bernhardt 2006; Neiman et al. 2008; Mueller et al. 2017). Mueller et al. (2017) examined in depth the influence of particular terrain features in inland-penetrating moisture transport associated with this AR, finding that while the most efficient pathway for moisture penetration was through the Columbia River "gap" region [i.e., the region between Mt. Adams and Mt. Hood as defined in Mueller et al. (2017)], most of the regionwide total inland moisture transport was due to the exceptionally strong and deep AR moisture overtopping parts of the mountain barrier itself. Recent studies have highlighted additional inland locations across the U.S. Intermountain West vulnerable to the effects of inland-penetrating ARs, including the south-central Idaho mountains, the Great Basin region (spanning portions of Nevada, Utah, and western Colorado), and southern Arizona along the Mogollon Rim (Alexander et al. 2015; Rutz et al. 2014, 2015; Swales et al. 2016). The mountains in south-central Idaho are of particular interest in this work, based on their proximity to the November 2006 AR-affected regions, as well as the region's known risk for flooding (Maddox et al. 1980; Idaho Office of Emergency Management 2011).

Climate change may alter many of the aforementioned characteristics of ARs, and the effect of climate change on ARs has been studied via a number of different approaches and datasets. The consensus among many recent global climate model (GCM) analyses indicates that ARs affecting the western United States will increase both in frequency and intensity, leading to increases in heavy precipitation (e.g., Dettinger 2011; Lavers et al. 2013; Gao et al. 2015; Lavers et al. 2015; Warner et al. 2015; Hagos et al. 2016). Many of these studies find that future AR-driven heavy precipitation will increase primarily through the "thermodynamic effect" (i.e., precipitation increases in response to Clausius–Clapeyron-modulated increases in atmospheric water holding capacity; Held and Soden 2006), which will also increase AR freezing level heights in addition to AR intensity (e.g., Dettinger 2011; Lavers et al. 2013; Gao et al. 2015; Lavers et al. 2015; Warner et al. 2015; Hagos et al. 2016). While the thermodynamic effect appears to dominate the climate change impact on ARs according to most studies (Kossin et al. 2017), location changes via dynamical effects related to the projected poleward shift of the subtropical jet would affect specific regions differently (e.g., Gao et al. 2015).

Regional climate model studies largely corroborate the changes indicated by global models, but impart additional spatial, temporal, and impact-relevant detail. For example, Salathé et al. (2014) used a regional dynamical downscaling approach to demonstrate that increases in future flood risk in many Pacific Northwest river basins are due to both more extreme and earlier (in the season) storms, and warming temperatures that shift precipitation from snow to rain. Other regional studies also demonstrate that increases in AR intensity and temperature are likely to produce more winter precipitation in the form of rain as opposed to snow, and that such a trend would increase flood risk particularly at higher elevations in complex terrain during intense landfalling AR events (e.g., Leung et al. 2004; Leung and Qian 2009; Guan et al. 2016).

A still finer-scale assessment of future inland-penetrating AR details and impacts can be achieved by the pseudo–global warming (PGW) modeling approach, whereby a present-day simulation of an event or period of interest is compared to a future realization of that same event, with GCM-indicated thermodynamic changes imposed (e.g., Schär et al. 1996; Frei et al. 1998; Kawase et al. 2009; Lackmann 2013; Rasmussen et al. 2014). A growing body of recent work highlights the PGW method and related event- and process-based "storytelling" types of model approaches for their ability to complement and add physical insight to the larger spatial- and temporal-scale context provided by global and regional models (e.g., Hazeleger et al. 2015; Lackmann 2015; Shepherd 2016; Matthews et al. 2018). We thus employ the PGW approach to investigate possible changes in moisture transport and pathways for the November 2006 inland-penetrating AR flood event.

We select the November 2006 Pacific Northwest event because it was an intense inland-penetrating AR that caused extensive flooding and we wish to evaluate the potential for intensification or modification of such types of events in a warmer climate. While an event-based PGW method affords valuable gains in spatial and temporal resolution, its trade-off is a limited sample size

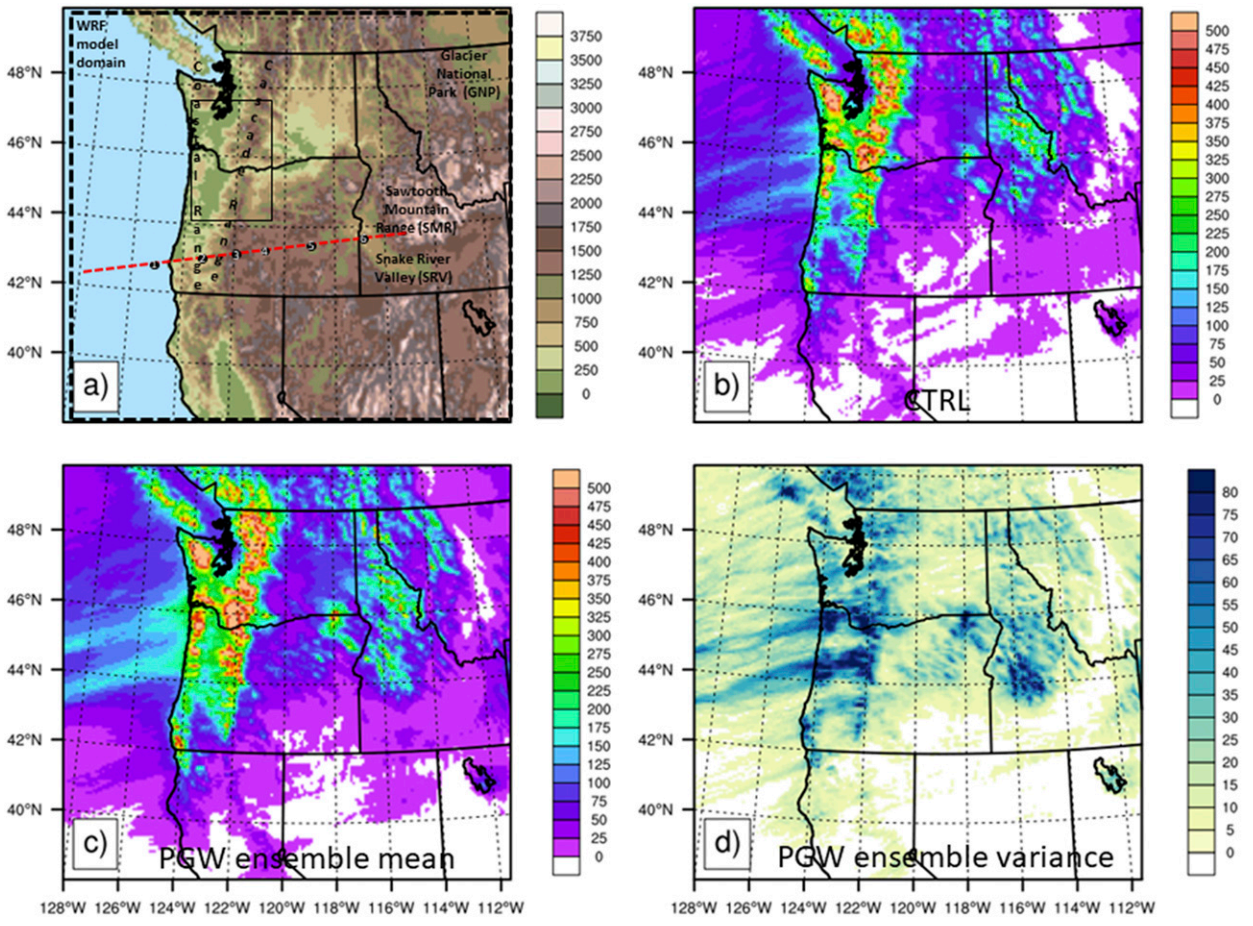

FIG. 1. (a) WRF Model domain (shown in its entirety inside dashed black line bordering panel) and terrain (m, as shown in color bar at right); inner black box denotes region used for calculating thermodynamic perturbations from the CESM LENS, black dots 1–6 denote locations used in Fig. 6, and red dashed line shows cross section used in Fig. 5. (b) CTRL total precipitation (mm, as shown in color bar at right). (c) As in (b), but for the PGW ensemble mean. (d) Variance among six PGW members (mm, as shown in color bar at right).

of event types studied. Although we only investigate a single event in this study, we produce multiple PGW simulations in order to better capture the range of uncertainty in such an event's response to imposed thermodynamic changes. Using an ensemble of PGW simulations of this event, we investigate how changes in future thermodynamic conditions may influence 1) precipitation intensity and spatial distribution both at AR landfall and inland locations, 2) moisture transport pathways, 3) specific components of moisture transport (i.e., change in wind relative to changes in moisture), and 4) the distribution of rain versus frozen precipitation and its possible implications for future flood risk.

2. Methods

The model simulations used in this study employ the Advanced Research Weather Research and Forecasting (WRF-ARW) modeling system, version 3.8.1 (Skamarock et al. 2008). The model domain uses 4-km grid spacing (Fig. 1a) and 54 vertical levels; the 4-km grid spacing affords the omission of convective parameterization and sufficiently resolves flow through finescale terrain features such as the Columbia River Gorge (Mueller et al. 2017). All simulations are run from 0000 UTC 3 November to 0000 UTC 9 November 2006, and initial and lateral boundary conditions are provided by 6-hourly Climate Forecast System Reanalysis (CFSR) data (Saha et al. 2010), with updating sea surface temperatures permitted. Other relevant model physics choices include Thompson microphysics (Thompson et al. 2008), the Yonsei University (YSU; Hong et al. 2006) planetary boundary layer, Monin–Obukhov surface layer, Dudhia shortwave radiation (Dudhia 1989), Rapid Radiative Transfer Model (RRTM; Mlawer et al. 1997) longwave radiation scheme, and the Noah land surface model (Ek et al. 2003). A "present day" simulation that is nearly identical (differing only in the present study's inclusion of updating sea

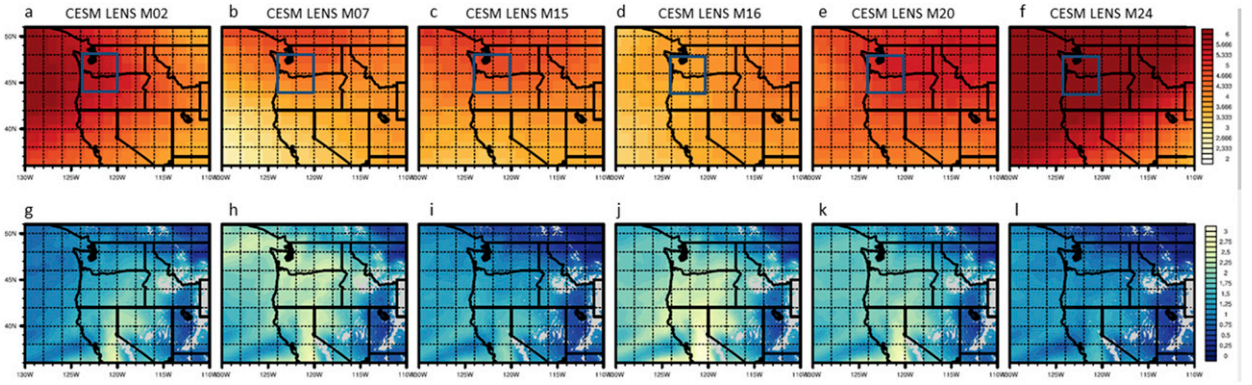

FIG. 2. (a) Change in temperature (ΔT) averaged over the 900–800-hPa layer as calculated from CESM LENS for M02 (°C as in color bar at bottom; areas in white indicate 900–800-hPa layer is below ground). Inner blue boxes denote region used for averaging and subsequent ranking of thermodynamic perturbations. (b) As in (a), but for CESM LENS member M07; (c) as in (a), but for CESM LENS member M15; (d) as in (a), but for CESM LENS member M16; (e) as in (a), but for CESM LENS member M20; (f) as in (a), but for CESM LENS member M24. (g)–(l) As in (a)–(f), but from the WRF simulation initial condition showing the resulting change in specific humidity (dq) as calculated from imposed temperature perturbation (ΔT; as detailed in section II) between 900 and 800 hPa (g kg^{-1} as in color bar at bottom).

surface temperatures) to the control (CTRL) run used here is described and analyzed in detail by Mueller et al. (2017).

The "future climate" simulations are produced using the pseudo–global warming method. This method combines the synoptic pattern of an observed event with climate model–indicated future large-scale thermodynamic changes imposed; many authors have shown the value of this approach in understanding how future thermodynamic climate-scale changes may impact a particular type of weather event or period of interest (e.g., Schär et al. 1996; Frei et al. 1998; Kawase et al. 2009; Lackmann 2013; Rasmussen et al. 2014). Because the PGW method focuses on a future incarnation of the large-scale synoptic weather pattern that led to a specific historical event and does not address the potential for changes in frequency, storm track, or intensity of additional possible future events, event-based PGW simulations cannot fully address the question of AR impacts in a future climate. However, the PGW approach (also referred to as the "delta method") does provide the additional strength of removing the mean model bias (by taking the mean difference between periods), as well as providing a robust estimate of the climate change signal (as opposed to natural variability), and has been used in many decision-making and stakeholder applications (e.g., Auad et al. 2006; Hare et al. 2012; Lynch et al. 2014; Zhang et al. 2016; Dominguez et al. 2018). Thus, to specifically evaluate potential inland impacts from a strong AR setup under climate warming, the PGW approach can offer valuable insight. The technique used here follows that of Lackmann (2013) and others, imposing a mean monthly climate model–determined temperature perturbation upon control simulation initial and lateral boundary conditions.

The climate model simulations used to determine these perturbations are from the 30-member NCAR CESM Large Ensemble (LENS; Kay et al. 2015), all run under the RCP8.5 scenario. We perform PGW simulations using six CESM LENS members, which are chosen based on the magnitude of their projected future changes in temperature and moisture over a Pacific Northwest subregion (Fig. 2), and the spread of which offers a manifestation of internal climate variability (Deser et al. 2012). For LENS member selection, monthly temperature and moisture perturbations are determined by differencing those fields at each grid point and model vertical level across future (2070–79) and present (1990–99) time periods. To highlight changes in low-level thermodynamics, which we expect are most likely to directly influence low-level moisture transport and precipitation, perturbation values are averaged between 900 and 800 hPa and then sorted. Member selection criteria were driven by the desire to capture a relatively wide range for climatic change and thus the six members chosen represent a spread across maximum, minimum, and median values of low-level temperature and specific humidity perturbations over the Pacific Northwest subregion (Fig. 2, Table 1). While the members were chosen based on maximum, minimum, and median values of temperature and humidity change over the Pacific Northwest subregion, the spatial pattern of the perturbation fields is heterogeneous across the domain (see Figs. S1–S3 in the online supplemental material) and so it is not anticipated or intended that changes in the resulting downscaled simulations

TABLE 1. CESM LENS member notation, perturbation descriptions, and occurrence of Sawtooth Mountain Range (SMR) precipitation increase [maximum (max), minimum (min), and median (med)].

CESM LE member (M) number	Description of large-scale thermodynamic perturbation averaged over Pacific Northwest subregion	Sawtooth Mountain Range precipitation increase?
CTRL (n/a)	None	—
M02	Max Q increase	N (SMR_0)
M07	Max T increase	N
M15	Min Q increase	Y (SMR+)
M16	Med Q increase	Y
M20	Med T increase	Y
M24	Min T increase	Y

should necessarily correspond in sign or intensity to the subregion-averaged magnitude of the change applied. In a recent PGW inland-penetrating AR study, Dominguez et al. (2018) applied thermodynamic changes homogeneously across the entire model domain; while the homogeneous approach somewhat simplifies interpretation of results, it is also arguably not as realistic a pattern of future warming.

The November mean temperature perturbation field is then added to the CFSR initial and boundary conditions at each respective grid point and vertical model level, with the (perturbed) boundary conditions updated every six hours for the duration of the simulation. Consistent with many previous studies, relative humidity is held constant such that water vapor mixing ratio increases in warmed locations following the Clausius–Clapeyron relationship; this control also allows for the use of the Clausius–Clapeyron relation to calculate a measure of the thermodynamically driven moisture adjustment (e.g., Frei et al. 1998; Held and Soden 2006; Lackmann 2013; Marciano et al. 2015). By constraining the system in this way [e.g., $\mathrm{RH} \equiv e(T + \Delta T, q)/e_s(T + \Delta T) = \text{const}$], we can compute a measure of the moisture adjustment, Δq, from a prescribed temperature perturbation, ΔT. The initial temperature perturbations from the six CESM LENS ensemble members are shown in Figs. 2a–f (with additional detail shown in Figs. S1–S4), whereas the corresponding WRF initial condition moisture fields derived from the imposed temperature perturbations are shown in Figs. 2g–l. While changes in moisture do not necessarily equate to changes in precipitation, the fixed relative humidity framework adopted here provides a qualitative estimate of the relative thermodynamic and dynamic contributions to changes in moisture transport and thus, to some degree, precipitation.

Finally, as discussed by Schär et al. (1996) and described in more detail by Lackmann (2013; 2015), small initial condition imbalances introduced by the PGW method are mitigated by allowing ample spinup time (approximately 36 h before initial AR landfall) and by using the WRF preprocessing system (WPS) to recompute geopotential height from the modified initial conditions such that the model initial state is hydrostatically balanced. Gravity wave adjustment between the wind and mass fields early in the simulation is accordingly short-lived. To confirm that small initial condition dynamical perturbations do not influence simulation outcomes, tests were further undertaken using the WRF digital filter initialization (DFI) procedure (Lynch and Huang 1992, 1994; Chen and Huang 2006; Peckham et al. 2016). This function uses an adiabatic backward and diabatic forward integration in order to fully balance the wind fields at the initial time, and employing it for PGW member test cases produced precipitation amounts and patterns nearly identical to those in the simulations in which the DFI procedure was not used (not shown).

3. Results

a. *Precipitation changes*

The storm-total precipitation from the "present day" control simulation compares well with available observations over both coastal Oregon and Washington State as well as at various inland locations (Mueller et al. 2017). Here our focus is how the CTRL simulation compares to the PGW ("future") experiments.

Each of the six PGW members demonstrates increases in overall precipitation, with concentrated swaths of enhanced precipitation extending from the Pacific Ocean inland to the Cascade Mountains (Fig. 3) and more generally eastward across the Pacific Northwest. Ensemble mean event-total precipitation differences between CTRL and the PGW simulations exceed 150 mm across large portions of western Oregon and Washington and central Idaho in particular (changes upward of 200% in some regions; see Fig. S5). There is a more subtle increase in the PGW ensemble mean precipitation across northern Idaho and Montana, including

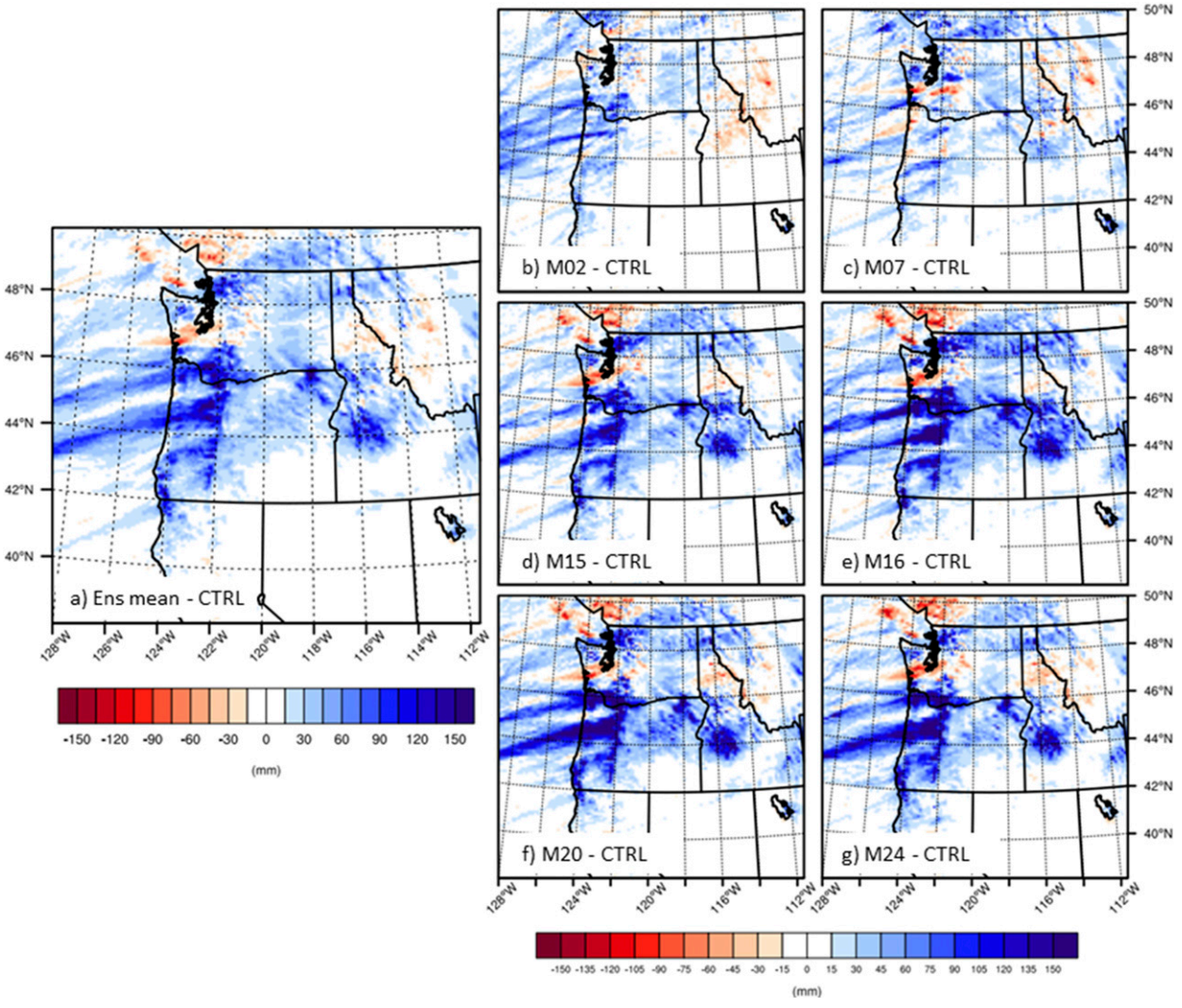

FIG. 3. (a) PGW ensemble mean minus CTRL total precipitation difference (mm, as shown in color bar at bottom). Remaining panels are as in (a), but for PGW members (b) M02, (c) M07, (d) M15, (e) M16, (f) M20, and (g) M24.

the GNP region in extreme northwestern Montana where the 2006 flooding was observed. Although all PGW simulations result in a marked overall domain-wide increase in event-total precipitation, relatively localized regions of decreases are also found, mainly across southwestern Canada, north-central Idaho/western Montana, and a narrow swath south of the Puget Sound. The regional decreases are attributable to a modest southward displacement in the main synoptic forcing in the PGW simulations, also evident in low-level jet axis and AR location discussed further below; similar timing and equatorward spatial offsets are observed in other PGW studies of frontal precipitation (e.g., Lackmann 2013; Marciano et al. 2015).

While the ensemble mean precipitation differences show a relatively coherent and strong signal, there are regions of notable variance among the PGW members. Figure 1d indicates regions of large PGW member spread around western Oregon and southern Washington State, as well as inland over south-central Idaho. The large variance over south-central Idaho is indicative of the prominent increase in precipitation around the Sawtooth Mountain Range (SMR) in four of the six members (M15, M16, M20, and M24), and absent in two members (M02 and M07) (Fig. 3, Table 1). Reasons for the variability over the SMR in particular are further investigated below.

Precipitation totals in many places increase at a rate far exceeding the Clausius–Clapeyron-indicated rate of ~7% $°C^{-1}$. Even for the PGW members with the largest temperature perturbations applied (6°–7°C; Fig. 2), localized super-Clausius–Clapeyron rates of precipitation

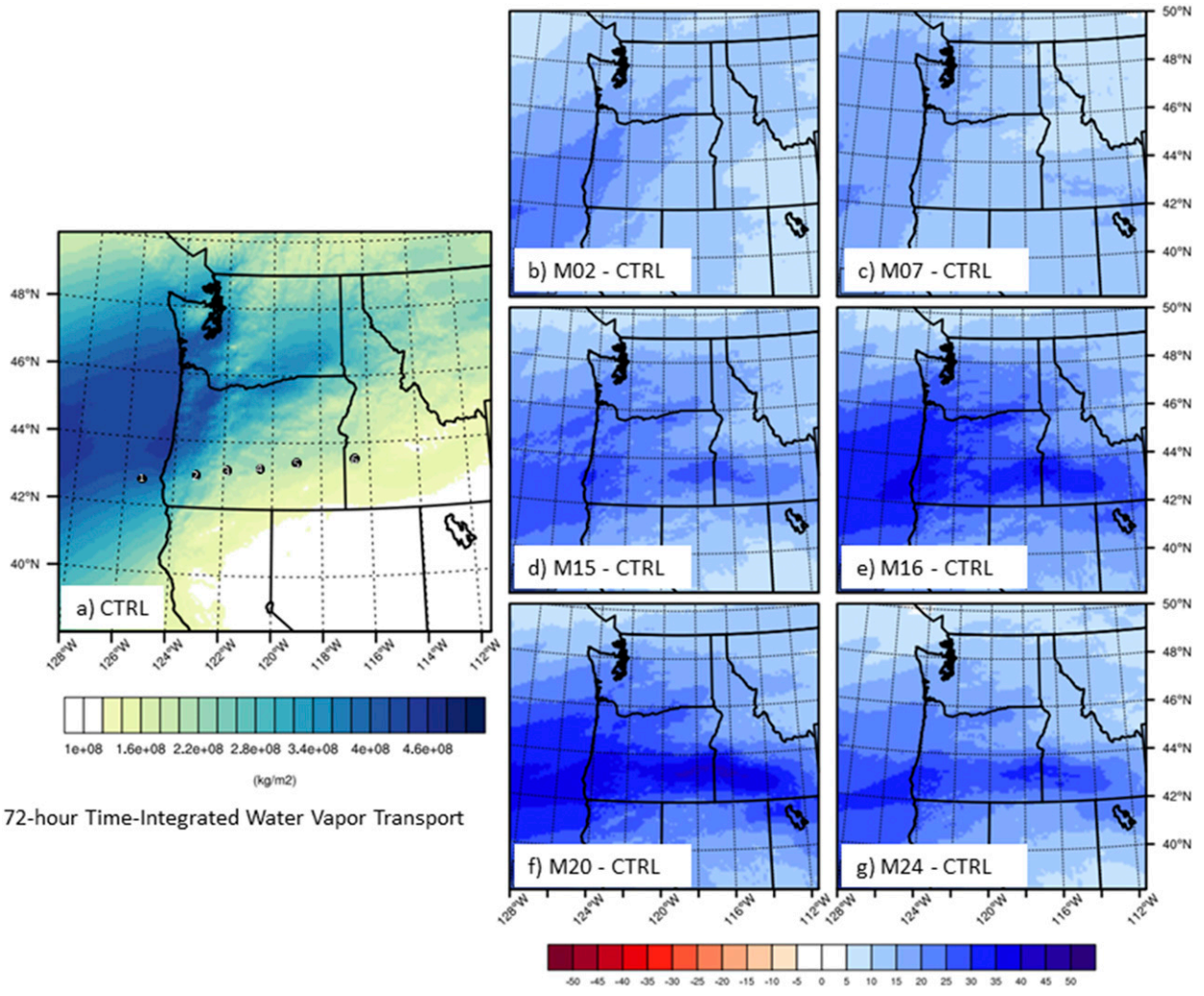

FIG. 4. (a) CTRL time-integrated water vapor transport 1200 UTC 5 Nov to 1200 UTC 8 Nov 2006 (kg m^{-2}, as shown in color bar at bottom); black dots 1–6 denote locations used in Fig. 6. (b) PGW M02 − CTRL total water vapor transport as percentage increase over CTRL (%, as shown in color bar at bottom. (c)–(g) As in (b), but for PGW members M07, M15, M16, M20, and M24, respectively.

enhancement are still noteworthy. While it is beyond the scope of this study to fully investigate the rates observed here, these results are largely consistent with the findings of many recent studies that highlight the sensitivity of observed and simulated extreme precipitation scaling relative to the theoretical calculated thermodynamic rate (O'Gorman 2015, and references therein). Further investigation of this case may be particularly interesting with respect to event temperature (e.g., for cool season cases, or temperatures below 295 K, enhanced precipitation efficiency has been found to explain nearly double Clausius–Clapeyron rates) and duration (e.g., many studies have shown an approximate doubling of precipitation rates when considering local subdaily and hourly precipitation extremes) (O'Gorman 2015, and references therein).

b. *Changes in moisture transport*

1) MOISTURE TRANSPORT INTENSITY AND PATHWAYS

A comparison of time-integrated, vertically integrated water vapor transport across all of the simulations summarizes the effects of increased moisture and enhanced dynamics (winds) in the PGW simulations relative to the CTRL. These storm-total moisture transport values, already large in the CTRL simulation, increase by up to 50% in some locations (Fig. 4). Of particular interest is the marked increase in PGW ensemble average precipitation over the SMR relative to the control simulation. The overall increase, plus the conspicuous absence of the SMR precipitation in two of

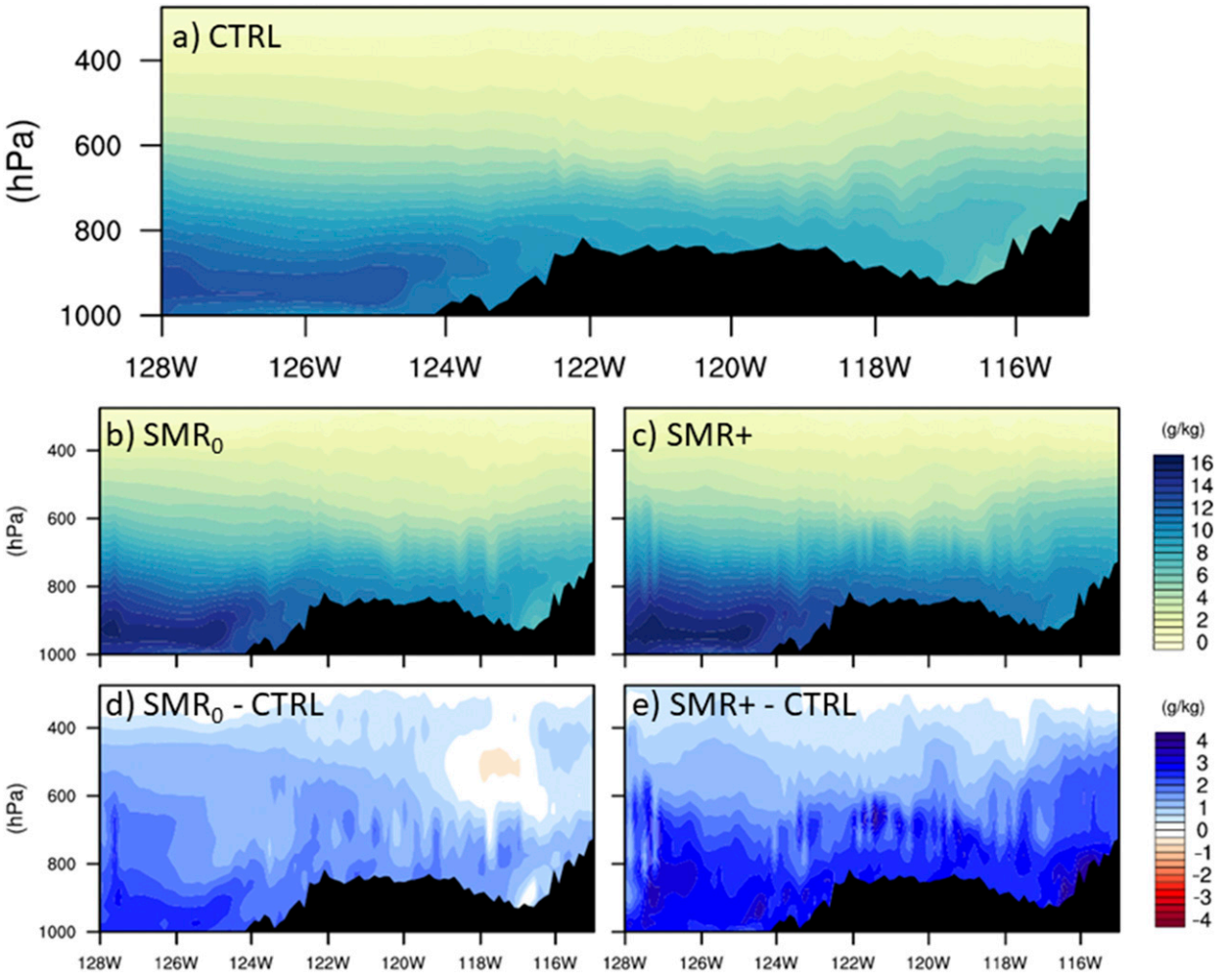

FIG. 5. (a) Specific humidity vertical cross section along southern Oregon transect shown in Fig. 1a at 0000 UTC 7 Nov for CTRL. (b) As in (a), but for SMR_0. (c) As in (a), but for SMR+. (d) SMR_0 − CTRL specific humidity difference (g kg^{-1}) shaded as in color bar at right. (e) As in (d), but for SMR+ − CTRL.

the PGW members and CTRL, suggests that moisture transport comparisons between the members may illuminate the critical factors in the SMR precipitation generation.

Comparing the accumulated water vapor transport through the Snake River Valley (SRV) immediately upwind of the SMR, shows that PGW members M15, M16, M20, and M24 (i.e., those *with* SMR precipitation enhancement) all possess a stronger eastward-directed, inland-penetrating corridor of moisture through central Oregon and into the SRV [relative to M02, M07, and CTRL (i.e., those *without* SMR precipitation enhancement); see Table 1] (Fig. 4). The aforementioned previous studies (e.g., Alexander et al. 2015, their Figs. 3 and 13; Rutz et al. 2015; Swales et al. 2016) linking south-central Idaho precipitation events to inland-penetrating ARs emphasize moisture transport by way of the California Central Valley and "northern Sierra," with a possible (less clear) secondary path directly from the west that would presumably describe a path "up-and-over" Oregon's coastal range. In this case, the AR's track is located well north of the California Central Valley pathway indicated by previous studies (e.g., Swales et al. 2016), so moisture transport via Northern California appears to be a less likely contributor to SRV moisture and SMR precipitation enhancement. Thus, for the PGW members that showed marked SMR enhancement, what did moisture transport and inland AR penetration look like over and around Oregon's elevated terrain?

A cross section spanning southern Oregon's elevated terrain from the coastline inland to the Snake River Valley at a time of peak AR intensity (0000 UTC 7 November) (Fig. 5) reveals a considerable increase in inland moisture depth and magnitude in M15 (a member representative of

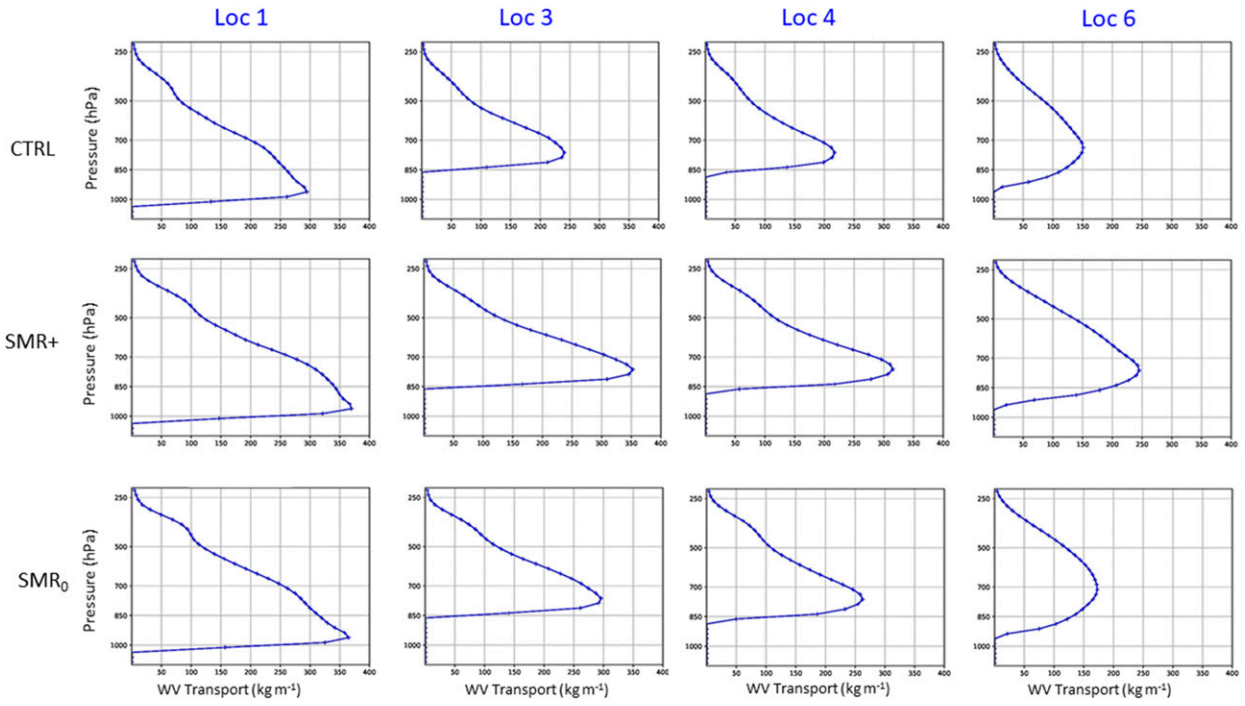

FIG. 6. Vertical profiles of time-integrated water vapor transport ($kg\,m^{-1}$) above points shown in Fig. 4.

the four PGW members *with* notable SMR precipitation enhancement; hereafter SMR+) relative to M02 (a member representative of those simulations *without* significant SMR enhancement; hereafter SMR_0; see Table 1). Figure 6 illustrates the vertical distribution of water vapor transport for the CTRL simulation, SMR_0, and SMR+ at locations of interest along a corridor encompassing offshore regions, central Oregon elevated terrain, and farther inland into the SRV. At location 1 offshore, moisture transport follows the same general temporal and vertical distribution across all members, although the PGW simulations have overall stronger moisture transport than CTRL (Fig. 6; see also Figs. S6 and S7). At location 3 along the western spine of the Cascades range, there is a significant increase in water vapor transport in SMR+ relative to CTRL and SMR_0. This same pattern of enhanced midlevel water vapor transport in the SMR+ relative to CTRL and SMR_0 continues across the inland, elevated terrain of southern Oregon illustrated by location 4. The water vapor transport distribution over location 6 in the SRV further reveals how much additional inland water vapor transport remained intact in SMR+ versus SMR_0 and CTRL. Particularly during the critical SMR precipitation period (0000 UTC 6 to 0000 UTC 8 November; Fig. S6), these PGW member differences in the vertical distribution of moisture transport (Fig. S7), the degree of maintenance of moisture transport intensity during the AR's inland penetration, and the resultant absolute moisture in the SRV and SMR at low to midlevels provide a clear explanation for why four of the PGW members did produce significant SMR precipitation while two members did not.

Figures 7 and 8 further summarize the evolution of moisture transport in SMR+ and SMR_0 across key time periods of AR landfall (Fig. 7) and inland penetration (Fig. 8). Time-integrated water vapor transport and mean vertically integrated water vapor over these periods illustrate the preferentially strengthened AR in SMR+ both offshore (Fig. 7) and inland (Fig. 8). SMR+ shows markedly more moisture (Figs. 7g,l) in the SMR, along with enhanced (and slightly southward displaced) low-level winds both along and directed into the SRV and SMR (Figs. 7h,m and 8h,m). The relative contributions of thermodynamic and dynamic effects are explored in more detail below.

To summarize, inland moisture transport intensities, depths, and pathways differ in the PGW simulations in multiple ways, each contributing to variation in SMR precipitation. First, for the PGW members generating heavier SMR precipitation, there is greater midlevel moisture transport over the southern Oregon terrain (Figs. 5 and 6). The increased intensity of midlevel moisture transport appears to be of primary importance and is consistent with a recent study of inland-penetrating AR midlevel water vapor transport by Backes et al. (2015). Second, the enhanced and slightly southward

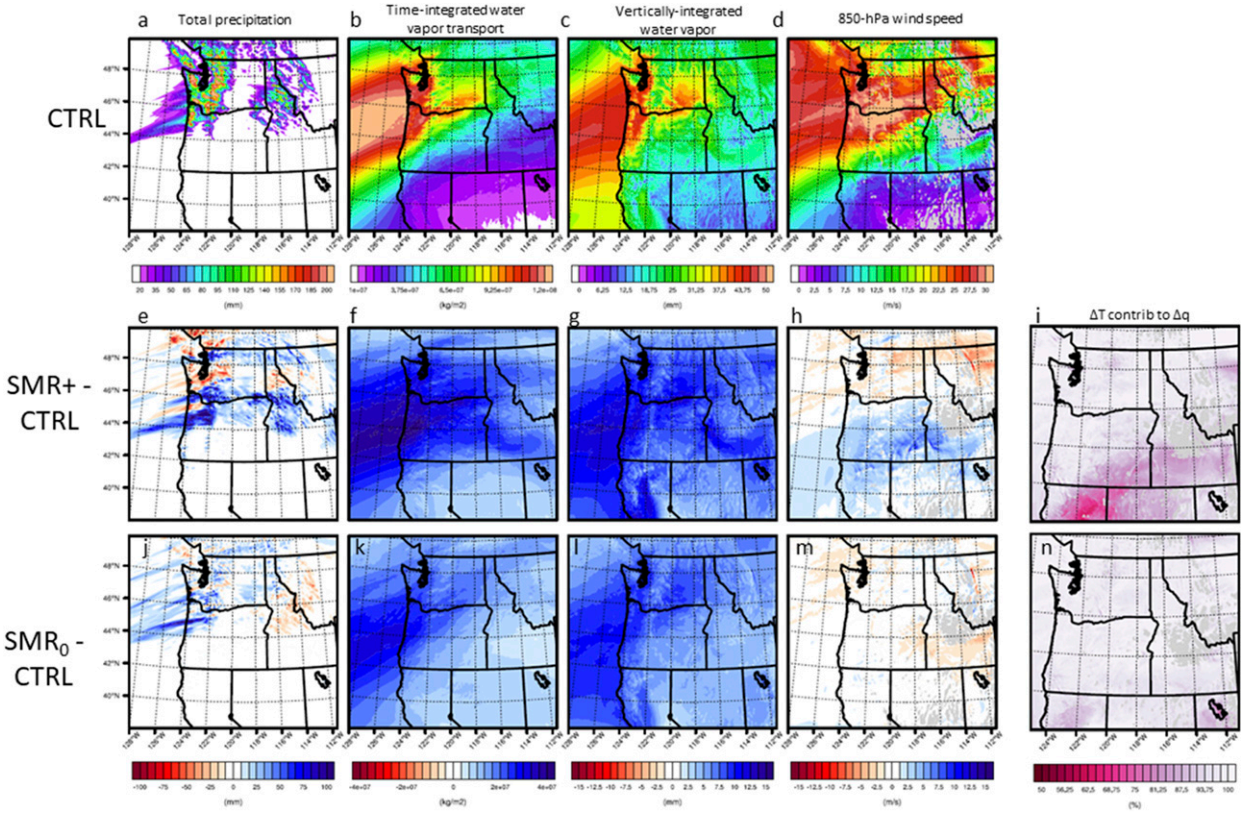

FIG. 7. All panels valid 0800 UTC 6 Nov (simulation hour 80) to 0400 UTC 7 Nov (simulation hour 100). Top panels show (a) CTRL total precipitation, (b) time-integrated total (vertically integrated) water vapor transport, (c) mean integrated water vapor, and (d) 850-hPa wind speed. In the middle is shown (e) SMR+ − CTRL precipitation difference (mm, as in color bar at bottom); other middle panels are as in (e), but for (f) total water vapor transport, (g) mean integrated water vapor, (h) 850-hPa wind speed, and (i) ΔT contribution to Δq (%, as in color bar at bottom; note that red colors indicate lower ΔT contribution and thus more dynamical contribution). (j)–(n) As in (e)–(i), but for SMR_0. Areas in gray denote where quantity is below ground.

displaced low- to midlevel winds provide persistent favorable terrain-relative flow through the SRV with which midlevel moisture is forced farther upward against the terrain to result in SMR orographic precipitation generation. Finally, the resultant increased moisture pooling in the SRV allows for prolonged precipitation generation in the SMR, and thus the PGW members with the largest increases in low to midlevel specific humidity in the SRV also generate the largest SMR increases in total precipitation.

2) THERMODYNAMIC- AND DYNAMICS-INFLUENCED CHANGES

Increased precipitation in the PGW simulations derive contributions from both increased lower-tropospheric water vapor (as prescribed by the PGW method) and enhanced dynamical mechanisms resulting from the changed background environment; the relative importance of each effect varies regionally and temporally throughout the event evolution. Because the PGW model simulations evolve dynamically over the course of the synoptic event, the PGW simulations as initially altered by prescribed thermodynamic changes do eventually include dynamical changes as well; thus a complete separation of the effects is not possible once a simulated event has evolved beyond its initial state. Still many studies have sought to separate and compare the two general mechanisms for precipitation enhancement, finding also that the relationship varies considerably by location and phenomena (e.g., Emori and Brown 2005; Sugiyama et al. 2010; Chou et al. 2012; Lackmann 2013; Pall et al. 2017). For this case, a simple comparison of simulated low-level moisture scaling relative to the theoretical values calculated from the Clausius–Clapeyron relationship suggests that, while much of the change in moisture across the domain is thermodynamically driven, the SMR precipitation is strongly controlled by inland low-level dynamics. As described in section 2, this distinction—highlighted in Figs. 7i,n and 8i,n by areas in which the saturation vapor pressure associated with the change in temperature (ΔT; of the PGW − CTRL) explains relatively less of the

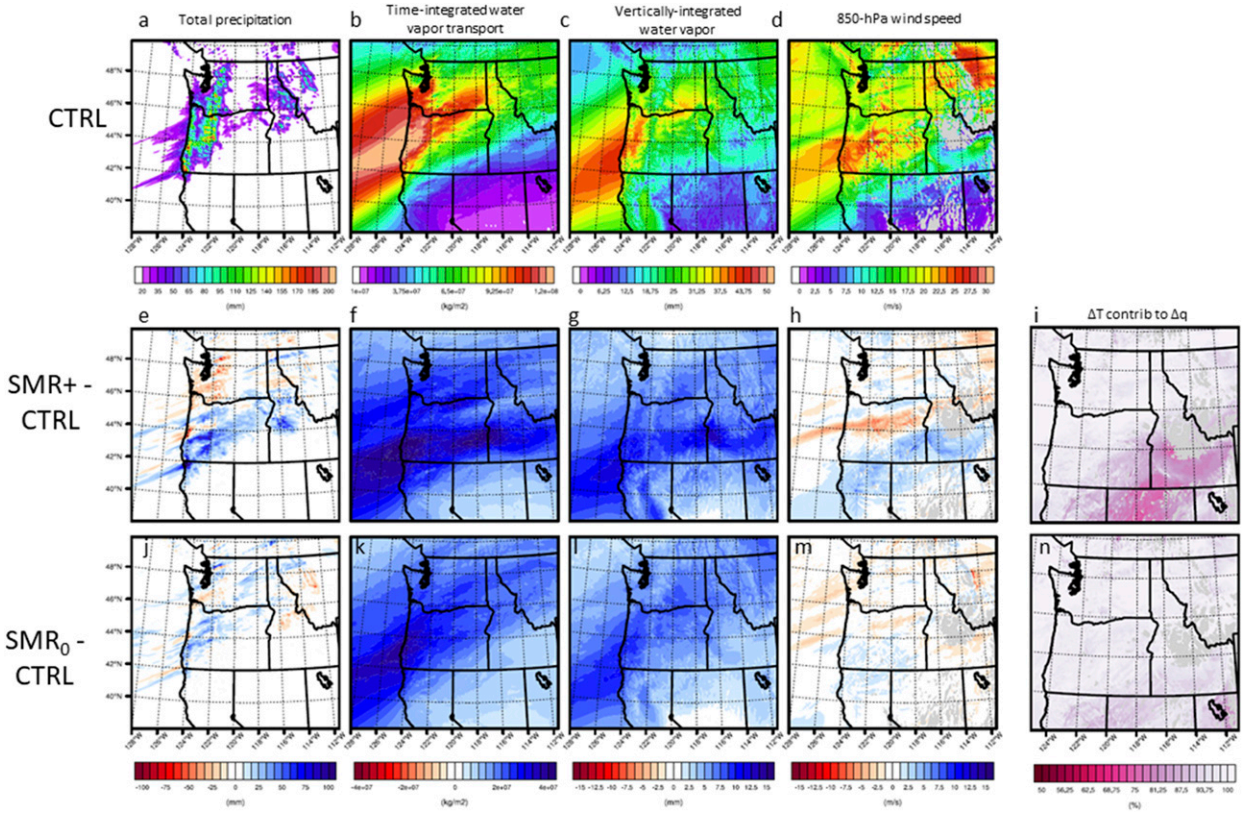

FIG. 8. As in Fig. 7, but valid for 0800 UTC 6 Nov (simulation hour 100) to 0400 UTC 7 Nov (simulation hour 120).

overall change in moisture (Δq; of the PGW member − CTRL)—suggests that changes in local dynamical mechanisms become key in determining localized inland precipitation amounts. Figures 7i and 8i specifically highlight the southern Oregon/Northern California region and farther inland to the SMR as areas in which the theoretical thermodynamic contribution to Δq is lower than the total change realized. Although a perfect separation of processes is not possible as explained above, this analysis does demonstrate that the total change in water vapor in these regions cannot be purely attributed to thermodynamic forcings, and that localized changes in dynamics (specifically changes in the low-level wind field) are of greater relative importance once the AR makes landfall and penetrates inland toward the SRV and SMR.

The symbiotic evolution of the changes in pure thermodynamics and local dynamics is further illustrated by comparing time-integrated water vapor transport and mean vertically integrated water vapor averaged over the time of initial AR landfall in Oregon (0800 UTC 6 to 0400 UTC 7 November, or simulation hours 80–100). The fields in tandem demonstrate the degree to which the AR has strengthened offshore, and that for SMR+ (and more generally, members with the largest precipitation increases overall), the time-integrated water vapor transport (cf. Figs. 7b,f,k) and low-level u wind (cf. Figs. 7d,h,m) are notably stronger in the AR's prefrontal warm sector (i.e., south of the AR across Oregon and Northern California). Critical to the generation of precipitation in the SMR specifically is the local low-level wind enhancement in this region (Fig. 7h). With more moisture in place (Fig. 7g), and steep terrain immediately downwind, this enhancement in SRV low-level wind speed leads to the generation of orographic precipitation in a location largely unaffected by precipitation in the present-day simulation. As the AR penetrates farther inland, precipitation increases in the SMR are less dramatic but still present. At this later time the precipitation appears to be due again to the enhanced moisture (Fig. 8g) but also, and perhaps more acutely, to the locally strengthened low-level winds along the California–Oregon border and into the SRV itself (Fig. 8h).

The conspicuous absence of the SMR precipitation enhancement in two of the PGW members (LENS members M02 or SMR_0 from above, and M07) is relatively interesting given that these members incidentally represent the more extreme "Max Q" and "Max T" thermodynamic changes observed in the CESM LENS

over the selection subregion. However, as discussed earlier, since ΔT is a heterogeneous field, computed and applied across each individual grid point and vertical level, the intensity and sign of ΔT in the Pacific Northwest specifically is just one of many factors affecting ensuing precipitation changes. A full explanation of each member's changes is beyond the scope of this study, but the interplay between stability effects, local precipitation processes, and moisture transport due to thermodynamic changes further afield is likely important, and these topics are more fully discussed in their own right in other studies of extreme events under climate change conditions (e.g., Hill and Lackmann 2011; Shi and Durran 2015, 2016; Pall et al. 2017). In summary, the dispersion found in the PGW simulation responses underscores the importance of understanding domain-wide thermodynamic shifts, as well as the potential added value of running high-resolution, event-based PGW simulations to capture nonlocal and/or nonlinear effects inherent to extreme precipitation environments.

c. *Distribution of rain versus snow, and implications for future flood risk*

While ARs are known to increase the environmental freezing level height through ample low-level warm advection, frozen precipitation still occurs in the CTRL simulation across much of the domain's highest terrain, notably across southwestern Canada, the northern Cascades, the SMR, and the northern Rocky Mountains. In the PGW simulations, however, warmer temperatures and higher freezing level heights result in a marked conversion from snow to rain at many of the higher-elevation and higher-latitude locations (Fig. 9; see also Figs. S8–S11). Consistent with overall atmospheric warming prescribed by the PGW perturbations, freezing level height (defined as the height above mean sea level of the 0°C isotherm) increases nearly everywhere in the domain; rises in the vicinity of elevated terrain are particularly notable both in their relative magnitude to lower elevations (Figs. S10 and S11) as well as in their potential to alter impacts and flood risk based on precipitation type (Fig. 10; see also Fig. S8). This resultant precipitation-type transition from frozen to liquid at higher elevations suggests the potential for decreased snowpack (which could, over the course of a season, lead to decreased water supply), as well as increased flood risk via instantaneous runoff generation as opposed to more gradual snowmelt processes.

While future frozen precipitation fractions decrease across the entire domain, the SMR/SRV region is again of special note for already being flood-prone in the present day (e.g., Maddox et al. 1980). The region contains many dams (https://www.idwr.idaho.gov/dams/) and climate-sensitive ecosystems (Klos et al. 2015) so intensified future heavy precipitation there may have particularly noteworthy flood risk implications. Additional factors must be accounted for in assessing total flood risk (e.g., Dominguez et al. 2018), but this finding provides higher-resolution, more detailed corroboration with the general findings of many observation-based and modeling studies focused on precipitation type and AR impacts in the western United States (e.g., Knowles et al. 2006; Leung and Qian 2009; Neiman et al. 2013; Salathé et al. 2014; Klos et al. 2015; Guan et al. 2016).

4. Conclusions

In this study we use pseudo–global warming (PGW) model simulations of a high-impact landfalling AR event in the U.S. Pacific Northwest to investigate potential future changes in moisture transport and precipitation intensity, type, and distribution. Specifically, we assess changes in 1) precipitation intensity and distribution both at AR landfall and inland locations, 2) moisture transport pathways, 3) specific components of moisture transport, and 4) the distribution of rain versus snow and its possible implications for future flood risk.

The results of the PGW model simulations show the following:

- Precipitation totals increase in all PGW simulations, most notably in offshore and coastal swaths upwind of the Coastal and Cascade Mountain Ranges of Oregon and Washington State, but also farther inland in locations such as Montana's Glacier National Park (GNP) and Idaho's Sawtooth Mountain Range (SMR). Precipitation totals in many locations increase at a rate far exceeding the Clausius–Clapeyron-indicated rate of $\sim$7% °C^{-1}.
- Four out of six of the PGW members show markedly increased precipitation in the SMR in south-central Idaho; this is particularly notable as this region had very little precipitation in the present-day (CTRL) simulation. In the SMR precipitation-enhancing members, moisture is shown to penetrate farther inland by more effectively crossing Oregon's Coastal and Cascade mountain ranges, essentially ''spilling over'' into the SRV and fueling orographic precipitation in the SMR.
- The regional changes leading to SMR precipitation enhancement represent a modification (or perhaps an extreme example) of the more southerly-storm-track-indicated south-central Idaho moisture transport pathway emphasized by previous studies (Rutz et al. 2014, 2015; Alexander et al. 2015; Swales et al. 2016). The processes shown here emphasize a primary shot of

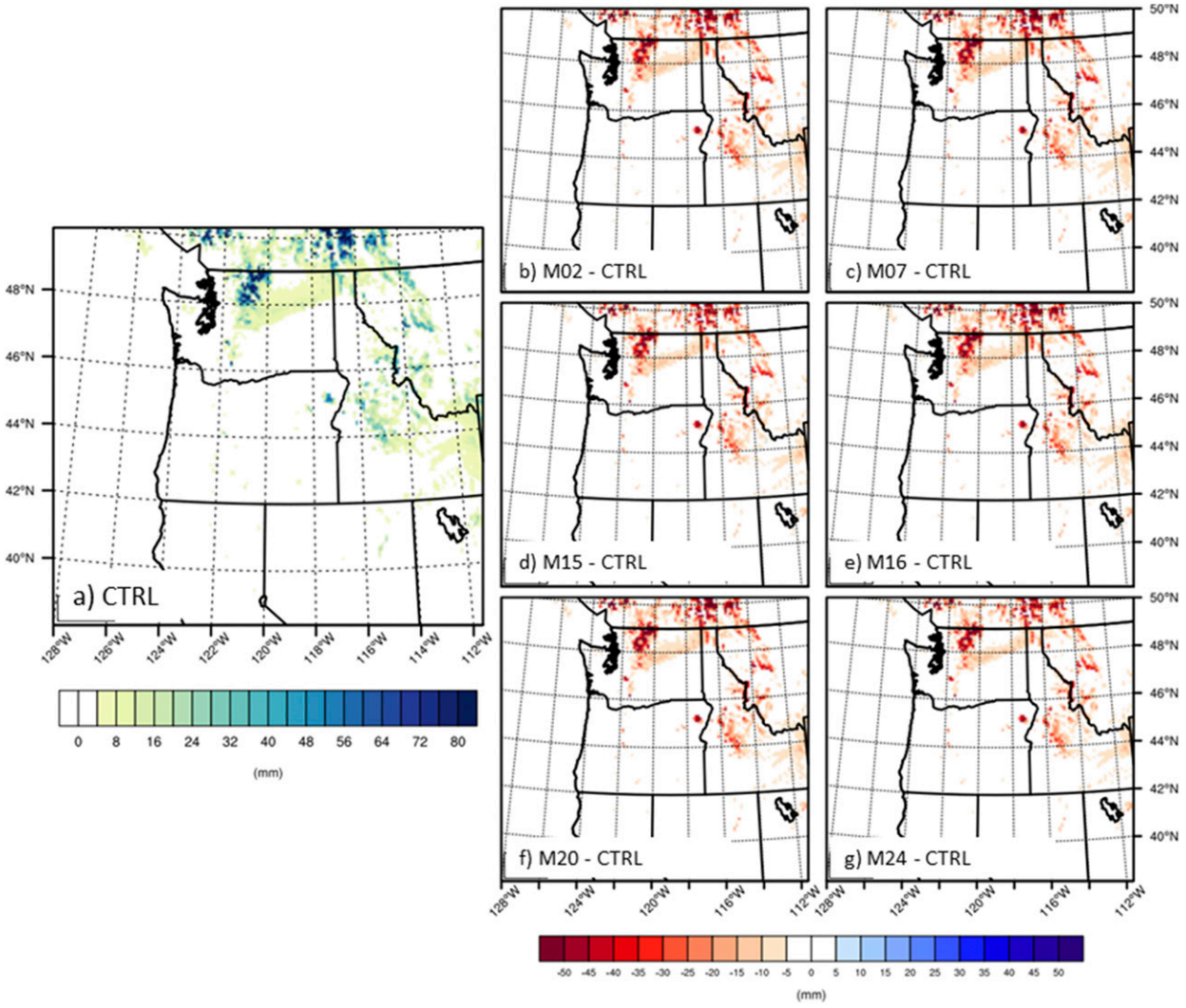

FIG. 9. (a) Total frozen precipitation (graupel + snow) in CTRL simulation (mm, shaded as in color bar at bottom). (b) PGW M02 − CTRL total frozen precipitation difference, as shown in color bar at bottom. (c)–(g) as in (b), but for PGW members M07, M15, M16, M20, and M24, respectively.

intense, zonal (westerly) moisture transport strong enough and deep enough to traverse the elevated terrain of western Oregon, with a later ''reinforcing'' dynamically driven intensification of moisture transport into the SRV by way of locally enhanced southwesterly winds extending from Northern California.

- PGW precipitation increases stem from enhanced moisture transport, which are in turn due to increases in both absolute moisture and lower-level and mid-level kinematic fields. For this case, the increase in domainwide precipitation initially derives largely from increased atmospheric moisture (as prescribed by the PGW method), with subsequent changes in local dynamics playing an important role further into the simulations as details of event evolution diverge across the various PGW environments. Low-level moisture transport ahead of the parent AR also strengthens in adjustment to the warmer, wetter atmosphere, and this appears to particularly augment inland moisture penetration to the SRV and SMR.
- Precipitation that fell as snow in the present-day CTRL simulation becomes rain in the PGW simulations for many mid- and high-elevation locations. This conversion suggests both potentially enhanced flood risk as well as ramifications for longer-term seasonal snowpack declines.
- Global climate model (NCAR CESM LENS) members selected for their most intense future changes in the western Washington region of primary interest did not lead to the most intense future precipitation

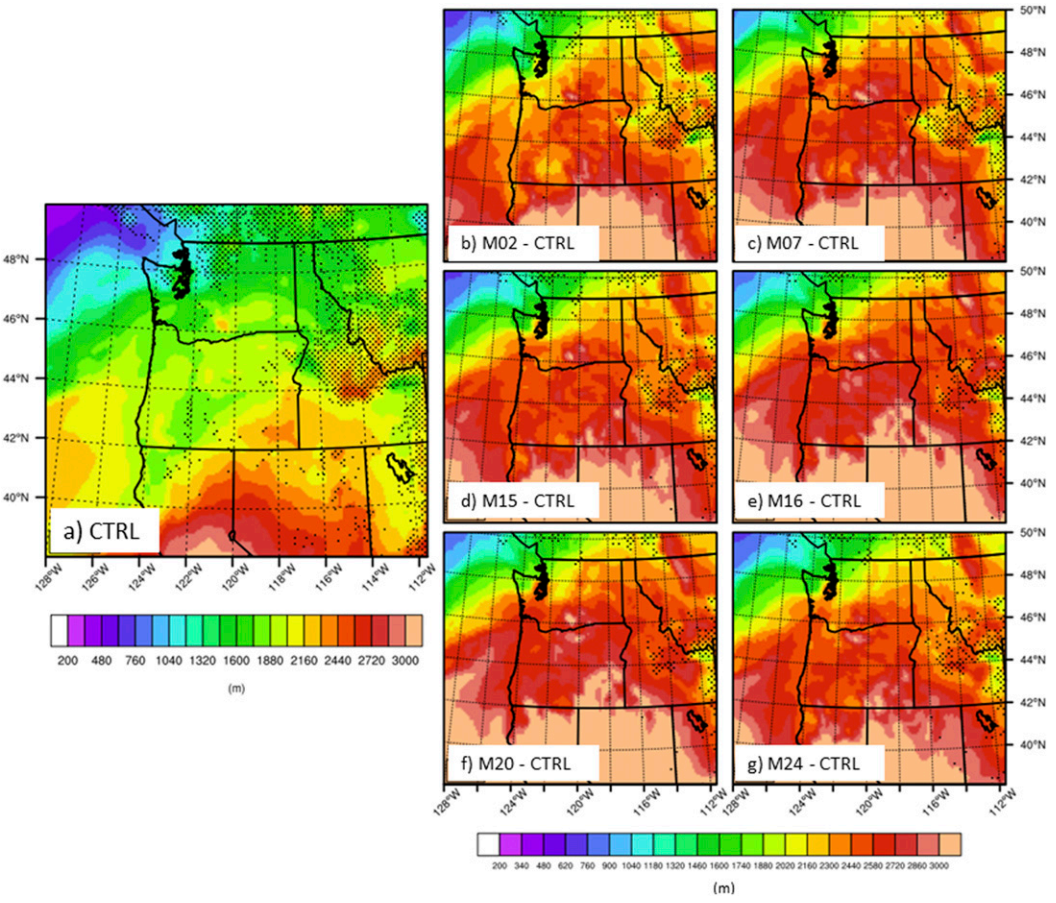

FIG. 10. (a) Freezing-level height at 0000 UTC 7 Nov (m above mean sea level, shaded as in color bar at bottom, where stippled areas denote regions where the freezing level is below ground). (b) As in (a), but for PGW M02. (c)–(g) As in (b), but for PGW members M07, M15, M16, M20, and M24, respectively.

intensification in the high-resolution PGW simulations. This suggests that the pattern of the changes applied is of significant importance to these types of simulations, and that further nonlinear/nonlocal responses (and thus valuable ensemble spread) can likely be achieved by growing the PGW ensemble by including perturbations calculated across either more LENS ensemble members or over other potentially influential regions.

Limitations to our study approach include the singularity of the case study examined, a lack of accounting for potential storm track shift (e.g., Gao et al. 2015; Shi and Durran 2015), and a limited (six member) set of PGW simulations/future thermodynamic changes considered. Additional cases, more inclusive of the spectrum of present-day event intensities, should also be investigated. While it is possible that some present-day strong events may weaken, the PGW simulation results suggest a mechanism by which climate change might also enhance the delivery of moisture to southern Idaho by enhancing the depth and intensity of more ''garden variety'' ARs. It is thus possible that in the future, weak or borderline flood events may become warmer, deeper, and more intense, potentially altering moisture pathways and differentially affecting other inland locations as seen in the SMR/SRV region here, or increasing the frequency and spatial extent of inland penetrating ARs in general. Further, as future thermodynamic changes are defined here using averaged climatological fields (i.e., the decadal average of a monthly mean), it is possible that future extreme events could instead evolve in environments that deviate strongly from these average changes. Thus, our approach quite possibly does not represent the most extreme instances of perturbation-influenced potential changes.

We have also briefly discussed that the conversion of snow to rain in many higher-elevation locations may increase flood risk. It is beyond the scope of this study to fully explore the hydrologic implications of such changes

but it is important to note that while heavy rainfall increases one aspect of flood risk, land surface conditions related to snowpack, soil saturation, and land use also act as important controlling factors. All of these aspects must be considered in a comprehensive projection of future flood risk, and climate models are not particularly well suited to represent local-scale land surface features and interactions. A more in-depth, event-based future effort could use a dynamical hydrologic model and a spectrum of PGW "deltas" to perturb atmospheric and land surface variables alike to more fully evaluate potential changes in future runoff generation and flood scenarios (e.g., Dominguez et al. 2018).

To the degree that the PGW method captures the potential for future climate-driven changes, one can interpret the above results as an indicator of what could happen in wetter, warmer, future-climate instances of similar landfalling ARs in this region. Even if one questions the notion that the PGW simulations adequately represent future possible background environmental thermodynamic states, the variations on the event still present realistic alternative event environments and evolutions, and thus a potentially valuable framework for establishing the character of regional flood risk.

Acknowledgments. This publication was supported by the Physical Sciences Division, NOAA/ESRL. The authors thank the NOAA Ernest F. Hollings Undergraduate Scholarship program for K. Malloy's funding support, three anonymous reviewers, and Prof. Gary Lackmann for helpful comments and discussion. NCAR and the National Science Foundation (NSF) are acknowledged for the availability of the WRF Model. This work utilized the Janus supercomputer, which is supported by the National Science Foundation (Award CNS-0821794) and the University of Colorado Boulder. The Janus supercomputer is a joint effort of the University of Colorado Boulder, the University of Colorado Denver, and the National Center for Atmospheric Research.

REFERENCES

Alexander, M. A., J. D. Scott, D. Swales, M. Hughes, K. Mahoney, and C. A. Smith, 2015: Moisture pathways into the U.S. Intermountain West associated with heavy winter precipitation events. *J. Hydrometeor.*, **16**, 1184–1206, https://doi.org/10.1175/JHM-D-14-0139.1.

Auad, G., A. Miller, and E. Di Lorenzo, 2006: Long term forecast of oceanic conditions off California and biological implications. *J. Geophys. Res. Oceans*, **111**, C09008, https://doi.org/10.1029/2005JC003219.

Backes, T. M., M. L. Kaplan, R. Schumer, and J. F. Mejia, 2015: A climatology of the vertical structure of water vapor transport to the Sierra Nevada in cool season atmospheric river precipitation events. *J. Hydrometeor.*, **16**, 1029–1047, https://doi.org/10.1175/JHM-D-14-0077.1.

Bernhardt, D., 2006: Glacier National Park flooding November 2006. NWS Western Region Tech. Attachment 08-23, 15 pp., https://www.weather.gov/media/wrh/online_publications/talite/talite0823.pdf.

Chen, M., and X.-Y. Huang, 2006: Digital filter initialization for MM5. *Mon. Wea. Rev.*, **134**, 1222–1236, https://doi.org/10.1175/MWR3117.1.

Chou, C., C.-A. Chen, P.-H. Tan, and K.-T. Chen, 2012: Mechanisms for global warming impacts on precipitation frequency and intensity. *J. Climate*, **25**, 3291–3306, https://doi.org/10.1175/JCLI-D-11-00239.1.

Deser, C., R. Knutti, S. Solomon, and A. S. Phillips, 2012: Communication of the role of natural variability in future North American climate. *Nat. Climate Change*, **2**, 775–779, https://doi.org/10.1038/nclimate1562.

Dettinger, M. D., 2011: Climate change, atmospheric rivers and floods in California—A multimodel analysis of storm frequency and magnitude changes. *J. Amer. Water Resour. Assoc.*, **47**, 514–523, https://doi.org/10.1111/j.1752-1688.2011.00546.x.

Dominguez, F., and Coauthors, 2018: Tracking an atmospheric river in a warmer climate: From water vapor to economic impacts. *Earth Syst. Dyn.*, **9**, 249–266, https://doi.org/10.5194/esd-9-249-2018.

Dudhia, J., 1989: Numerical study of convection observed during the Winter Monsoon Experiment using a mesoscale two-dimensional model. *J. Atmos. Sci.*, **46**, 3077–3107, https://doi.org/10.1175/1520-0469(1989)046<3077:NSOCOD>2.0.CO;2.

Ek, M. B., K. E. Mitchell, Y. Lin, E. Rogers, P. Grunmann, V. Koren, G. Gayno, and J. D. Tarpley, 2003: Implementation of Noah land surface model advances in the National Centers for Environmental Prediction operational mesoscale Eta model. *J. Geophys. Res.*, **108**, 8851, https://doi.org/10.1029/2002JD003296.

Emori, S., and S. J. Brown, 2005: Dynamic and thermodynamic changes in mean and extreme precipitation under changed climate. *Geophys. Res. Lett.*, **32**, L17706, https://doi.org/10.1029/2005GL023272.

Frei, C., C. Schär, D. Lüthi, and H. C. Davies, 1998: Heavy precipitation processes in a warmer climate. *Geophys. Res. Lett.*, **25**, 1431–1434, https://doi.org/10.1029/98GL51099.

Gao, Y., J. Lu, L. R. Leung, Q. Yang, S. Hagos, and Y. Qian, 2015: Dynamical and thermodynamical modulations on future changes of landfalling atmospheric rivers over western North America. *Geophys. Res. Lett.*, **42**, 7179–7186, https://doi.org/10.1002/2015GL065435.

Guan, B., D. E. Waliser, F. M. Ralph, E. J. Fetzer, and P. J. Neiman, 2016: Hydrometeorological characteristics of rain-on-snow events associated with atmospheric rivers. *Geophys. Res. Lett.*, **43**, 2964–2973, https://doi.org/10.1002/2016GL067978.

Hagos, S. M., L. R. Leung, J.-H. Yoon, J. Lu, and Y. Gao, 2016: A projection of changes in landfalling atmospheric river frequency and extreme precipitation over western North America from the Large Ensemble CESM simulations. *Geophys. Res. Lett.*, **43**, 1357–1363, https://doi.org/10.1002/2015GL067392.

Hare, J. A., and Coauthors, 2012: Cusk (*Brosme brosme*) and climate change: Assessing the threat to a candidate marine fish species under the US Endangered Species Act. *ICES J. Mar. Sci.*, **69**, 1753–1768, https://doi.org/10.1093/icesjms/fss160.

Hazeleger, W., B. J. J. M. van den Hurk, E. Min, G. J. van Oldenborgh, A. C. Petersen, D. A. Stainforth, E. Vasileiadou, and L. A. Smith, 2015: Tales of future weather. *Nat. Climate Change*, **5**, 107–113, https://doi.org/10.1038/nclimate2450.

Held, I. M., and B. J. Soden, 2006: Robust responses of the hydrological cycle to global warming. *J. Climate*, **19**, 5686–5699, https://doi.org/10.1175/JCLI3990.1.

Hill, K. A., and G. M. Lackmann, 2011: The impact of future climate change on TC intensity and structure: A downscaling approach. *J. Climate*, **24**, 4644–4661, https://doi.org/10.1175/2011JCLI3761.1.

Hong, S.-Y., Y. Noh, and J. Dudhia, 2006: A new vertical diffusion package with an explicit treatment of entrainment processes. *Mon. Wea. Rev.*, **134**, 2318–2341, https://doi.org/10.1175/MWR3199.1.

Hughes, M., K. M. Mahoney, P. J. Neiman, B. J. Moore, M. Alexander, and F. M. Ralph, 2014: The landfall and inland penetration of a flood-producing atmospheric river in Arizona. Part II: Sensitivity of modeled precipitation to terrain height and atmospheric river orientation. *J. Hydrometeor.*, **15**, 1954–1974, https://doi.org/10.1175/JHM-D-13-0176.1.

Idaho Office of Emergency Management, 2011: Idaho Floods!: A Flood Awareness Guide for the Gem State. 43 pp., https://ioem.idaho.gov/Pages/Preparedness/Hazards/NaturalHazards/Flood.aspx.

Kawase, H., T. Yoshikane, M. Hara, F. Kimura, T. Yasunari, B. Ailikun, H. Ueda, and T. Inoue, 2009: Intermodel variability of future changes in the Baiu rainband estimated by the pseudo global warming downscaling method. *J. Geophys. Res.*, **114**, D24110, https://doi.org/10.1029/2009JD011803.

Kay, J. E., and Coauthors, 2015: The Community Earth System Model (CESM) Large Ensemble Project: A community resource for studying climate change in the presence of internal climate variability. *Bull. Amer. Meteor. Soc.*, **96**, 1333–1349, https://doi.org/10.1175/BAMS-D-13-00255.1.

Klos, P. Z., and Coauthors, 2015: Indicators of climate change in Idaho: An assessment framework for coupling biophysical change and social perception. *Wea. Climate Soc.*, **7**, 238–254, https://doi.org/10.1175/WCAS-D-13-00070.1.

Knowles, N., M. D. Dettinger, and D. R. Cayan, 2006: Trends in snowfall versus rainfall in the western United States. *J. Climate*, **19**, 4545–4559, https://doi.org/10.1175/JCLI3850.1.

Kossin, J. P., T. Hall, T. Knutson, K. E. Kunkel, R. J. Trapp, D. E. Waliser, and M. F. Wehner, 2017: Extreme storms. Climate Science Special Report: Fourth National Climate Assessment, Vol. I, D. J. Wuebbles et al., Eds., U.S. Global Change Research Program, 257–276, https://doi.org/10.7930/J07S7KXX.

Lackmann, G. M., 2013: The south-central U.S. flood of May 2010: Present and future. *J. Climate*, **26**, 4688–4709, https://doi.org/10.1175/JCLI-D-12-00392.1.

——, 2015: Hurricane Sandy before 1900 and after 2100. *Bull. Amer. Meteor. Soc.*, **96**, 547–560, https://doi.org/10.1175/BAMS-D-14-00123.1.

Lavers, D. A., R. P. Allan, G. Villarini, B. Lloyd-Hughes, D. J. Brayshaw, and A. J. Wade, 2013: Future changes in atmospheric rivers and their implications for winter flooding in Britain. *Environ. Res. Lett.*, **8**, 034010, https://doi.org/10.1088/1748-9326/8/3/034010.

——, F. M. Ralph, D. E. Waliser, A. Gershunov, and M. D. Dettinger, 2015: Climate change intensification of horizontal water vapor transport in CMIP5. *Geophys. Res. Lett.*, **42**, 5617–5625, https://doi.org/10.1002/2015GL064672.

Leung, L. R., and Y. Qian, 2009: Atmospheric rivers induced heavy precipitation and flooding in the western U.S. simulated by the WRF regional climate model. *Geophys. Res. Lett.*, **36**, L03820, https://doi.org/10.1029/2008GL036445.

——, ——, X. Bian, W. M. Washington, J. Han, and J. O. Roads, 2004: Mid-century ensemble regional climate change scenarios for the western United States. *Climatic Change*, **62**, 75–113, https://doi.org/10.1023/B:CLIM.0000013692.50640.55.

Lynch, P., and X.-Y. Huang, 1992: Initialization of the HIRLAM model using a digital filter. *Mon. Wea. Rev.*, **120**, 1019–1034, https://doi.org/10.1175/1520-0493(1992)120<1019:IOTHMU>2.0.CO;2.

——, and ——, 1994: Diabatic initialization using recursive filters. *Tellus*, **46A**, 583–597, https://doi.org/10.1034/j.1600-0870.1994.t01-4-00003.x.

——, J. A. Nye, J. A. Hare, C. A. Stock, M. A. Alexander, J. D. Scott, K. L. Curti, and K. Drew, 2014: Projected ocean warming creates a conservation challenge for river herring populations. *ICES J. Mar. Sci.*, **72**, 374–387, https://doi.org/10.1093/icesjms/fsu134.

Maddox, R. A., F. Canova, and L. R. Hoxit, 1980: Meteorological characteristics of flash flood events over the western United States. *Mon. Wea. Rev.*, **108**, 1866–1877, https://doi.org/10.1175/1520-0493(1980)108<1866:MCOFFE>2.0.CO;2.

Marciano, C. G., G. M. Lackmann, and W. A. Robinson, 2015: Changes in U.S. East Coast cyclone dynamics with climate change. *J. Climate*, **28**, 468–484, https://doi.org/10.1175/JCLI-D-14-00418.1.

Matthews, T., C. Murphy, G. McCarthy, C. Broderick, and R. L. Wilby, 2018: Super Storm Desmond: A process-based assessment. *Environ. Res. Lett.*, **13**, 014024, https://doi.org/10.1088/1748-9326/aa98c8.

Mlawer, E. J., S. J. Taubman, P. D. Brown, M. J. Iacono, and S. A. Clough, 1997: Radiative transfer for inhomogeneous atmospheres: RRTM, a validated correlated-k model for the longwave. *J. Geophys. Res.*, **102**, 16 663–16 682, https://doi.org/10.1029/97JD00237.

Mueller, M., K. M. Mahoney, and M. R. Hughes, 2017: High-resolution model-based investigation of moisture transport into the Pacific Northwest during a strong atmospheric river event. *Mon. Wea. Rev.*, **145**, 3861–3879, https://doi.org/10.1175/MWR-D-16-0466.1.

Neiman, P. J., F. M. Ralph, G. A. Wick, Y.-H. Kuo, T.-K. Wee, Z. Ma, G. H. Taylor, and M. D. Dettinger, 2008: Diagnosis of an intense atmospheric river impacting the Pacific Northwest: Storm summary and offshore vertical structure observed with COSMIC satellite retrievals. *Mon. Wea. Rev.*, **136**, 4398–4420, https://doi.org/10.1175/2008MWR2550.1.

——, ——, B. J. Moore, M. Hughes, K. M. Mahoney, J. Cordeira, and M. D. Dettinger, 2013: The landfall and inland penetration of a flood-producing atmospheric river in Arizona. Part I: Observed synoptic-scale, orographic, and hydrometeorological characteristics. *J. Hydrometeor.*, **14**, 460–484, https://doi.org/10.1175/JHM-D-12-0101.1.

Newell, R. E., N. E. Newell, Y. Zhu, and C. Scott, 1992: Tropospheric rivers?—A pilot study. *Geophys. Res. Lett.*, **19**, 2401–2404, https://doi.org/10.1029/92GL02916.

O'Gorman, P. A., 2015: Precipitation extremes under climate change. *Curr. Climate Change Rep.*, **1**, 49–59, https://doi.org/10.1007/s40641-015-0009-3.

Pall, P., C. M. Patricola, M. F. Wehner, D. A. Stone, C. J. Paciorek, and W. D. Collins, 2017: Diagnosing conditional anthropogenic contributions to heavy Colorado rainfall in September 2013. *Wea. Climate Extremes*, **17**, 1–6, https://doi.org/10.1016/j.wace.2017.03.004.

Peckham, S. E., T. G. Smirnova, S. G. Benjamin, J. M. Brown, and J. S. Kenyon, 2016: Implementation of a digital filter initialization in the WRF Model and its application in the Rapid

Refresh. *Mon. Wea. Rev.*, **144**, 99–106, https://doi.org/10.1175/MWR-D-15-0219.1.

Rasmussen, R., and Coauthors, 2014: Climate change impacts on the water balance of the Colorado headwaters: High-resolution regional climate model simulations. *J. Hydrometeor.*, **15**, 1091–1116, https://doi.org/10.1175/JHM-D-13-0118.1.

Rutz, J. J., W. J. Steenburgh, and F. M. Ralph, 2014: Climatological characteristics of atmospheric rivers and their inland penetration over the western United States. *Mon. Wea. Rev.*, **142**, 905–921, https://doi.org/10.1175/MWR-D-13-00168.1.

——, ——, and ——, 2015: The inland penetration of atmospheric rivers over western North America: A Lagrangian analysis. *Mon. Wea. Rev.*, **143**, 1924–1944, https://doi.org/10.1175/MWR-D-14-00288.1.

Saha, S., and Coauthors, 2010: The NCEP Climate Forecast System Reanalysis. *Bull. Amer. Meteor. Soc.*, **91**, 1015–1057, https://doi.org/10.1175/2010BAMS3001.1.

Salathé, E. P., A. F. Hamlet, C. F. Mass, S.-Y. Lee, M. Stumbaugh, and R. Steed, 2014: Estimates of twenty-first-century flood risk in the Pacific Northwest based on regional climate model simulations. *J. Hydrometeor.*, **15**, 1881–1899, https://doi.org/10.1175/JHM-D-13-0137.1.

Schär, C., C. Frei, D. Lüthi, and H. C. Davies, 1996: Surrogate climate-change scenarios for regional climate models. *Geophys. Res. Lett.*, **23**, 669–672, https://doi.org/10.1029/96GL00265.

Shepherd, T. G., 2016: A common framework for approaches to extreme event attribution. *Curr. Climate Change Rep.*, **2**, 28–38, https://doi.org/10.1007/s40641-016-0033-y.

Shi, X., and D. R. Durran, 2015: Estimating the response of extreme precipitation over midlatitude mountains to global warming. *J. Climate*, **28**, 4246–4262, https://doi.org/10.1175/JCLI-D-14-00750.1.

——, and ——, 2016: Sensitivities of extreme precipitation to global warming are lower over mountains than over oceans and plains. *J. Climate*, **29**, 4779–4791, https://doi.org/10.1175/JCLI-D-15-0576.1.

Skamarock, W. C., and Coauthors, 2008: A description of the Advanced Research WRF version 3. Tech. Rep. NCAR/TN-475+STR, 113 pp.

Sugiyama, M., H. Shiogama, and S. Emori, 2010: Precipitation extreme changes exceeding moisture content increases in MIROC and IPCC climate models. *Proc. Natl. Acad. Sci. USA*, **107**, 571–575, https://doi.org/10.1073/pnas.0903186107.

Swales, D., M. Alexander, and M. Hughes, 2016: Examining moisture pathways and extreme precipitation in the U.S. Intermountain West using self-organizing maps. *Geophys. Res. Lett.*, **43**, 1727–1735, https://doi.org/10.1002/2015GL067478.

Thompson, G., P. R. Field, R. M. Rasmussen, and W. D. Hall, 2008: Explicit forecasts of winter precipitation using an improved bulk microphysics scheme. Part II: Implementation of a new snow parameterization. *Mon. Wea. Rev.*, **136**, 5095–5115, https://doi.org/10.1175/2008MWR2387.1.

Warner, M. D., C. F. Mass, and E. P. Salathé, 2015: Changes in winter atmospheric rivers along the North American west coast in CMIP5 climate models. *J. Hydrometeor.*, **16**, 118–128, https://doi.org/10.1175/JHM-D-14-0080.1.

Zhang, C., Y. Wang, K. Hamilton, and A. Lauer, 2016: Dynamical downscaling of the climate for the Hawaiian Islands. Part II: Projection for the late twenty-first century. *J. Climate*, **29**, 8333–8354, https://doi.org/10.1175/JCLI-D-16-0038.1.